Continental Shelf Research 281 (2024) 105310

Contents lists available at ScienceDirect

Continental Shelf Research

journal homepage: www.elsevier.com/locate/csr

Upwelling processes variability and water circulation along the northern margin of the Gulf of Cadiz

Luciano de Oliveira Júnior [a,*], Paulo Relvas [b], Erwan Garel [a]

[a] Centre for Marine and Environmental Research (CIMA), University of Algarve, Faro, 8005-139, Portugal
[b] Centre of Marine Sciences (CCMAR), University of Algarve, Faro, 8005-139, Portugal

ARTICLE INFO

Keywords:
Ekman transport
Ekman pumping
Coastal upwelling
Coastal counter currents
Alongshore pressure gradient
Gulf of Cadiz

ABSTRACT

The present study investigates the contributions of upwelling mechanisms (coastal upwelling from boundary divergence and Ekman pumping from spatially variable wind) at the northern margin of the Gulf of Cadiz (NMGoC) based on high-resolution wind. The effects of the spatiotemporal upwelling mechanisms variability are then explored using current observations along with sea surface temperature and sea level anomaly. Upwelling favourable conditions occur throughout the year along the NMGoC, with the strongest intensity near Cape São Vicente due to a persistent positive wind stress curl. In winter, the surface water divergence is restricted to the coastal boundary due to strong coastal upwelling events that result in a cross-shore sea-level gradient close to the coast. Towards the summer, the gradient increases and extends further offshore (over the slope) at the western region due to the intensification of the Ekman pumping. Therefore, the seasonal and spatial variability of coastal upwelling and Ekman pumping contributes significantly to the offshore position of the geostrophic Gulf of Cadiz Current over the western shelf slope. Furthermore, a permanent sea level depression corresponds to the location of the strongest Ekman pumping, near Cape São Vicente. The dynamic adjustment of this feature may drive the cyclonic cell and alongshore poleward currents often observed in the area.

1. Introduction

Wind-driven coastal upwelling is an oceanic phenomenon resulting from the divergence of surface waters at the coastal boundary due to both alongshore winds and the earth's rotation. If the wind blows with the coast on its left (right) side in the northern (southern) hemisphere, it will promote a net transport of the upper layers of water 90° to the right (left) of the wind's direction, a process called Ekman transport. The water displaced offshore is then replaced by colder and nutrient-rich deeper waters in a relatively narrow coastal band. Since wind generally varies in space, so does the Ekman transport, and divergence (or convergence) arises in the ocean surface waters, forcing vertical velocities independently of the coastal boundary (Gill, 1982). This mechanism is often called Ekman pumping and is associated with positive (or negative) wind stress curl typical of regions with prominent topographic features. Both coastal Ekman transport (coastal upwelling hereafter) and Ekman pumping generally coexist. Some studies have quantified the contribution of each mechanism to the total upwelling in regions of intense upwelling activity. It was shown that, compared to coastal upwelling, Ekman pumping generally drives a comparatively weaker upwelling (or downwelling) over a much larger area that may extend hundreds of kilometres offshore (Capet et al., 2004). Nonetheless, when integrated over some distance offshore, vertical velocities from Ekman pumping results in transport with magnitudes comparable to those of coastal upwelling. At the California upwelling system, for example, the integration of Ekman pumping over 300 km offshore using modelled winds to resolve the curl associated with relatively small-scale topographic features revealed that it can be largely dominant over coastal upwelling (Pickett, 2003). At some specific locations, such as the southern California Bight, Ekman pumping associated with one of the major promontories in the California upwelling system was largely dominant. Such dominance was also demonstrated in other regions associated with prominent topographic features, such as along the south-eastern Brazilian coast (Castelao and Barth 2006), in Chile (Bravo et al., 2016) and in the south-eastern Arabian Sea (Jayaram and Jose, 2022).

The effect of Ekman pumping has also been demonstrated to be a determinant factor that controls other aspects of the water circulation. Castelao and Barth (2007) used a high-resolution numerical model to study the importance of spatial variability in the wind forcing to the

* Corresponding author.
E-mail address: lojunior@ualg.pt (L. de Oliveira Júnior).

https://doi.org/10.1016/j.csr.2024.105310
Received 16 May 2023; Received in revised form 4 August 2024; Accepted 12 August 2024
Available online 21 August 2024

separation of a coastal upwelling jet at Cape Blanco in the California upwelling system. Their results showed that, as positive wind stress curl drives Ekman pumping upwelling, which tilts isotherms upward in the offshore region, thus forcing southward current velocities via the thermal wind balance. Numerical experiments that include idealized and realistic scenarios also indicated that the gradient of wind stress curl promotes an alongshore pressure gradient that drives alongshore poleward flows in the Santa Barbara Channel (Oey, 1996, 1999). Moreover, the localized effect of Ekman pumping may cause an overall doming of the isopycnals in regions at some distance from the coast, which promotes a cyclonic circulation to compensate for the baroclinic pressure field (Di Lorenzo, 2003; Münchow, 2000; Wang, 1997).

At the Northern Margin of the Gulf of Cadiz (NMGoC), at the southern limit of the Iberian upwelling system, the effect of the wind stress curl associated with the orography at Cape São Vicente (CSV, Fig. 1) may also be relevant. Some authors suggested that the baroclinic compensation of curl-driven upwelling could be responsible for the recurrently observed cyclonic gyre in the NMGoC (Criado-Aldeanueva et al., 2006; de Oliveira Júnior et al., 2022; García-Lafuente et al., 2006). It was also argued that Ekman pumping near CSV could enhance local upwelling affecting the SST fields (Sánchez et al., 2007) and possibly promote an alongshore pressure gradient that drives coastal counter currents (CCCs) poleward (Sánchez et al., 2006).

Although some efforts have been made to estimate the effect of curl-driven upwelling in the NMGoC (Alvarez et al., 2008; Castelao and Luo, 2018; Criado-Aldeanueva et al., 2006; Sánchez-Leal et al., 2020; Sánchez and Relvas, 2003), no study has been designed specifically to understand and characterize its variability in the region and to evaluate its direct impact on the circulation. Previous assessments of curl-driven upwelling in the NMGoC were mainly based on satellite scatterometer data which cover areas relatively far from the coast and lack sufficient resolution to resolve small-scale wind patterns associated with the presence of CSV. In the present study, winds from SKIRON - a high spatial (5 km) and temporal (1 h) resolution model - are used to estimate the upwelling intensity from both wind-driven processes, coastal upwelling and Ekman pumping. The main objective is to differentiate upwelling due to surface water divergence associated with the coastal boundary from upwelling due to a spatially variable wind field. It is noted that both phenomena generally coexist and may overlap as they result from the same physical process (Ekman transport). Yet, the analysis of the spatiotemporal upwelling variability at a given water depth along the coast, induced by modulations of wind curl or coastal divergence contributions, may provide insights about the regional circulation drivers. To derive the main conclusions, the patterns obtained from the estimated processes are compared with ancillary sea surface temperature (SST), sea level anomaly (SLA) and current observations. It is shown that Ekman pumping is an important factor for the circulation in the NMGoC, affecting both shelf and slope currents as it enhances upwelling and shapes the sea level slope in both the alongshore and cross-shore directions.

2. Background to the area

2.1. Geographical setting

The NMGoC lays along the southern Atlantic coast of Portugal and Spain. It extends from CSV, where the coastline orientation changes from meridional to zonal at the southwest tip of the Iberian Peninsula, to the Strait of Gibraltar in the east (Fig. 1). The region's topography is marked by the presence of a zonally orientated coastal mountain range. The continental shelf consists of two distinct physiographic elements separated by Cape Santa Maria, where the shelf is the narrowest (5 km

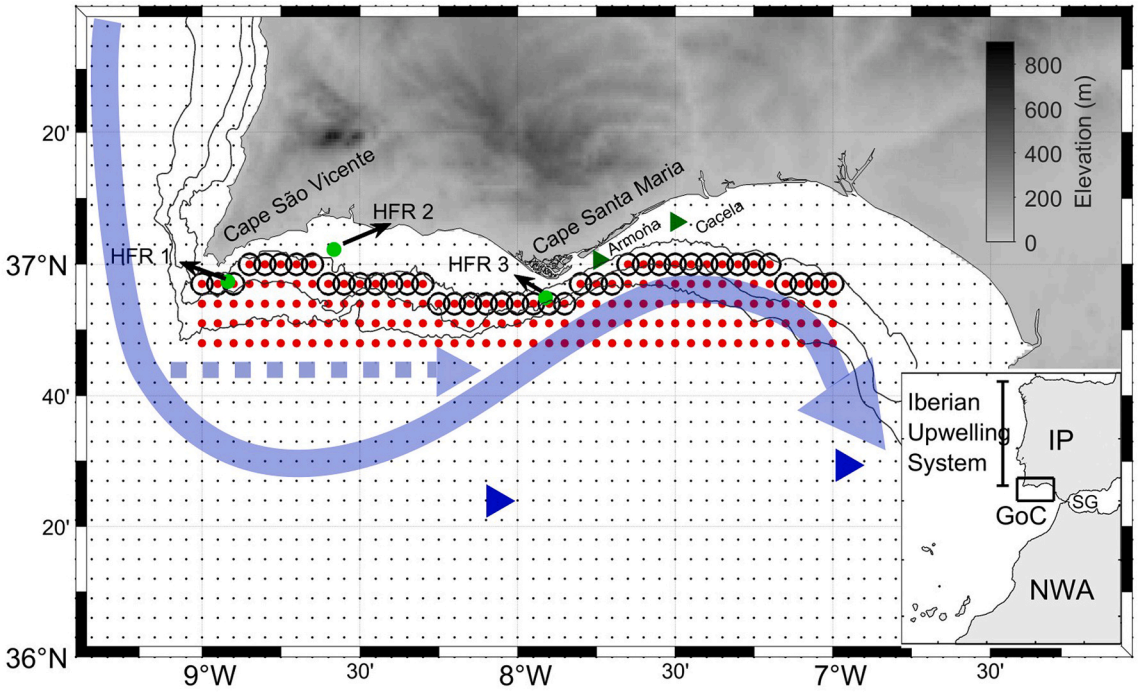

Fig. 1. Study area showing the SKIRON grid nodes (black dots). The black circles indicate the grid nodes nearest to the 50 m isobath where the cross-shore transport due to the coastal upwelling ($\boldsymbol{Ek_{Ty}}$) was extracted for comparison with the Ekman pumping transport ($\boldsymbol{EkP_T}$). Red dots represent nodes from the 50 m isobath to the fixed offshore latitude of 36°48′ N representative of the shelf slope region where Ekman pumping velocities ($\boldsymbol{w_{Ek}}$) were integrated to compute $\boldsymbol{EkP_T}$ (see section 3.4). Blue triangles indicate the locations of the in-situ wind measurements used to validate modelled wind data. Green (dark green) dots (triangles) represent the position of in-situ surface (depth-averaged) currents from HFR (ADCP) observations. Black arrows indicate the name of each HFR station. The isobaths of 50 m, 100 m and 200 m are represented as thin black lines. The faint blue arrows depict the seasonal pathways of the Gulf of Cadiz Current (GCC) described in de Oliveria Júnior et al., (2022), with the solid (dashed) line representing summer (winter). The land topography is represented in shades of grey. For the general location, see inset (IP: Iberian Peninsula; NWA: northwest of Africa; GoC: Gulf of Cádiz; SG: Strait of Gibraltar).

wide): a western bight, characterised by a relatively narrow shelf (<30 km) with a steep slope, and an eastern bight where the shelf is comparatively wider (>40 km), and the slope is gentler (Fig. 1). The shelf break roughly corresponds to the 200 m isobath.

2.2. Wind patterns

The wind regime in the NMGoC region is mainly regulated by the Azores anticyclonic high-pressure cell position and intensity (Chase, 1951). During spring and summer (from March to August, typically), the Azores high displace north, increasing the pressure difference between the centre of the anticyclone and the Iberian Peninsula. This atmospheric set up produces a dominant wind regime characterized by relatively strong northerlies along the west coast of Portugal and at the Gulf of Cádiz entrance (Fiúza et al., 1982; Mazé et al., 1997). Due to the development of a thermal low in the centre of the Iberian Peninsula (Hoinka and De Castro, 2003) and to the presence of the coastal mountain range (Fiúza, 1983; Relvas and Barton, 2002), the northerlies rotate anticlockwise to north-westerlies towards the east of the gulf (de Oliveira Júnior et al., 2021; Sánchez and Relvas, 2003). During winter, the Azores High displaces southward and weakens while the Iceland Low intensifies. This pattern favours the development of westerlies and an increased number of frontal systems that cause an overall variable wind regime in the region (Chase, 1951; Losada, 1999).

Another recurrent wind pattern that is often observed in the region is the so-called "Levanter" produced by a variety of atmospheric set up (Losada, 1999; Trigo and DaCamara, 2000) but is highly controlled by the complex interaction of the wind with the local topography at the Strait of Gibraltar (Capon, 2006; Dorman et al., 1995). Levanter typically blows from the east or southeast (Peliz et al., 2009b, 2014) along the NMGoC without clear seasonality (de Oliveira Júnior et al., 2021; Ribas-Ribas et al., 2011).

2.3. Circulation patterns

Observations and numerical experiments have shown the existence of an equatorward current (so-called the Gulf of Cadiz Current, GCC hereafter) along the continental slope of the NMGoC all year round (Cravo et al., 2013; Criado-Aldeanueva et al., 2006, 2009; de Oliveira Júnior et al., 2022; García-Lafuente et al., 2006; Garcia et al., 2002; Peliz et al., 2007, 2009a, 2009b). Over the western bight, the GCC magnitude and width are seasonally modulated (see faint blue arrows in Fig. 1), being strong and extending significantly offshore in summer but weak and restricted to the upper slope in winter (de Oliveira Júnior et al., 2022; García-Lafuente et al., 2006). Over the eastern bight, the flow veers anticyclonically following the slope orientation (Criado-Aldeanueva et al., 2006, 2009; Fiúza, 1983; Garcia et al., 2002; Peliz et al., 2007, 2009a; Relvas and Barton, 2002; Sánchez and Relvas, 2003). The flow is often described as the continuation of the geostrophic upwelling jet developing along the western coast that turns cyclonically at CSV to conserve potential vorticity (García-Lafuente et al., 2006; Relvas and Barton, 2002; Sánchez et al., 2006; Sánchez and Relvas, 2003). However, the GCC is observed year-round, contrary to the offshore Ekman transport (produced by persistent northerlies in summer), suggesting that other factors may drive this flow. For example, numerical simulations suggest that the GCC results from the interaction of the dense Mediterranean outflow and Atlantic inflow (Kida et al., 2008; Peliz et al., 2007, 2009a). Moreover, wind stress curl produced near CSV probably affects the slope circulation at the western bight during the upwelling season by producing local upwelling and stirring a mesoscale cyclonic eddy (Criado-Aldeanueva et al., 2006; de Oliveira Júnior et al., 2022; García-Lafuente et al., 2006; Sánchez et al., 2006, 2007; Sánchez and Relvas, 2003).

Near the coast, the circulation is characterized by polarised alongshore subtidal flows, which are generally balanced in the poleward (broadly westward) and equatorward (broadly eastward) directions (except in the vicinity of Cape Santa Maria where equatorward flows dominate) without seasonality (de Oliveira Júnior et al., 2021, 2022; Garel et al., 2016). Equatorward flows are generally associated with upwelling events, generated locally or remotely, and advect cold water over the margin (Fiúza, 1983; Relvas and Barton, 2002). High-frequency radar (HFR) observations show that these flows typically extend across the entire shelf and merge with the GCC (de Oliveira Júnior et al., 2022). By contrast, poleward flows are generally confined to the shelf and are associated with the advection of a narrow (about 20–30 km) band of water, warm in summer, leaning along the coast (de Oliveira Júnior et al., 2022; Fiúza, 1983; García-Lafuente et al., 2006; Relvas and Barton, 2002). Poleward flows are often referred to as CCCs as they have opposed directions to the permanent GCC over the slope (de Oliveira Júnior et al., 2022). These CCCs are produced by the imbalance of an alongshore pressure gradient during the relaxation (or reversal) of upwelling-favourable winds (García-Lafuente et al., 2006; Garel et al., 2016; Relvas and Barton, 2002; Sánchez et al., 2006) and are enhanced by Levanter (Teles-Machado et al., 2007). At the western bight, the CCCs and GCC form a cyclonic recirculation cell that develops during the relaxation of upwelling favourable winds (de Oliveira Júnior et al., 2022) and occupies most of the shelf and upper slope water column (García-Lafuente et al., 2006). At the eastern bight, scarce observations also support that the CCCs and GCC form a similar cyclonic cell (García-Lafuente et al., 2006).

3. Data and methods

3.1. Wind

Wind data was obtained from the regional weather forecasting system SKIRON, developed at the Hellenic National Meteorological Service (Kallos et al., 2006; Papadopoulos et al., 2002). SKIRON is a non-hydrostatic numerical weather prediction model (Janjic et al., 2001) that includes a 3D data assimilation package to produce 7 days forecasts of high-resolution (5 km) analysis fields (wind, air temperature, specific humidity, total cloud cover, sea level pressure, total precipitation, upward and downward long wave flux, evaporation, latent heat flux and sensible heat flux). For the present study, only the daily forecast outputs of hourly wind data at 10 m height (u and v components) for the 2013–2020 period are considered. Some files were corrupted during the downloading process, producing gaps in the time series up to 4 months in 2017. For unbiased seasonal comparisons, the entire year of 2017 was discarded (grey band in Fig. 2a). The remaining 75 gaps (dots in Fig. 2a) range from 2 h to 241 h (total of 2160 h, representing 3.6% of the considered time series), with most gaps (87%) shorter than 26 h (Fig. 2b).

For validation at the NMGoC, the u and v components of the SKIRON wind were compared with concomitant hourly measurements from the ASCAT scatterometer (on board of MetOp-A satellite) and two offshore buoys. ASCAT records were obtained from the daily L3 files at the Remote Sensing Systems website (https://remss.com/, last access January 10, 2023) in grids with 0.25° (28 km) spatial resolution which include measurements of u and v components and rain flags from both the descending and ascending passes. In-situ observations originate from the Faro buoy, which has been operating since 2014 at the centre of the Gulf of Cadiz, and the Cadiz buoy installed further east in 2008 (see Fig. 1). The measurements, at 3 m height, were extrapolated to 10 m considering a typical Hellmann exponential law. The validation was performed using approximately 5000 concomitant records from ASCAT, 39,134 records from the Faro buoy and 52,992 records from the Cadiz buoy.

The SKIRON outputs and measurements compare well (Fig. 3), with a Pearson's correlation coefficient (R) $\geq$ 0.7 for both the u and v components. In particular, the model reproduces accurately daily wind fluctuations (Fig. 3a and b). The weakest correlations are found for the ASCAT u component near CSV (R = 0.73, Fig. 3c), where northerlies

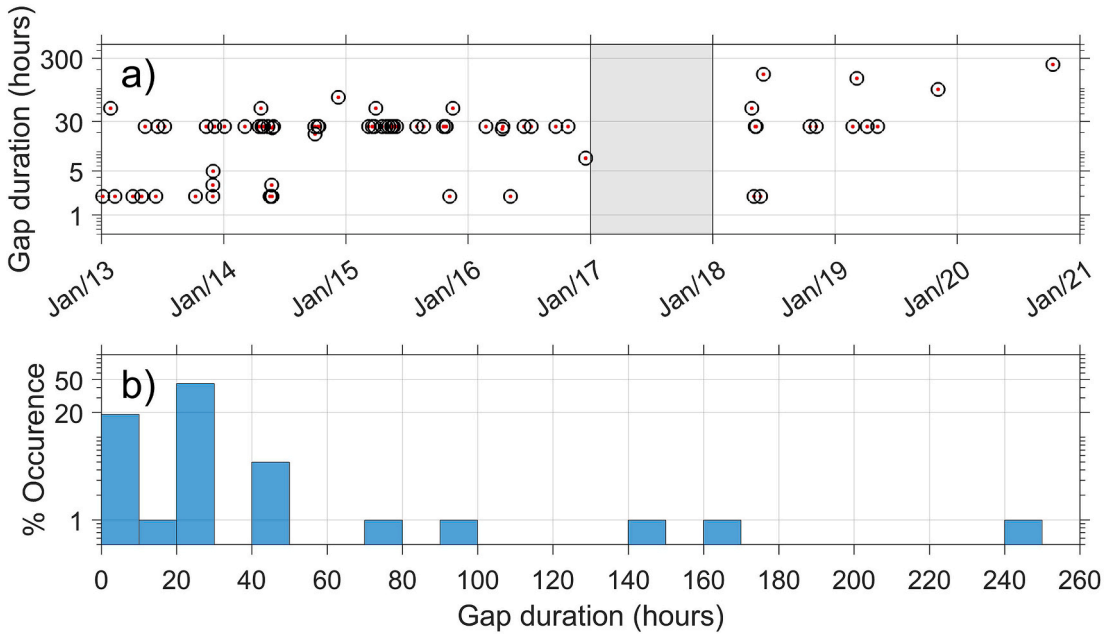

Fig. 2. SKIRON gaps duration throughout the considered time series (a). Percentage of occurrence of the gaps classed by durations of 10 h (b).

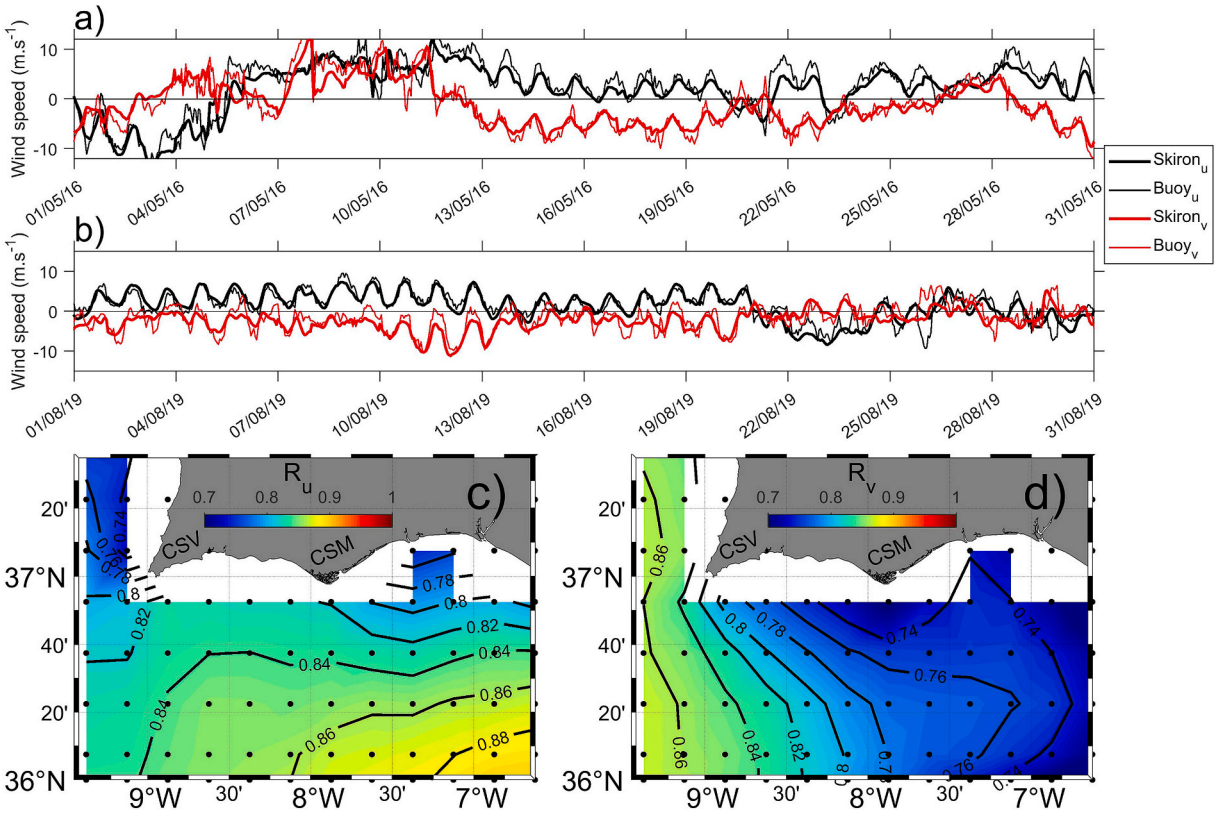

Fig. 3. Comparisons of SKIRON winds (thick lines) with buoy measurements (thin lines) at Faro buoy (a) and Cadiz buoy (b). Black (red) represents the u (v) component. Pearson's correlation coefficient between SKIRON and Ascat winds for the u (c) and v (d) components.

dominate, and near Cape Santa Maria (R = 0.7, Fig. 3d) where the v component is relatively weak. This overall good correlation between modelled and measured winds shows that SKIRON can reproduce reasonably well the main features associated with the wind variability over the NMGoC.

3.2. Ancillary data

Daily satellite altimeter SLA data produced by AVISO was downloaded from CMEMS (Copernicus Marine Environment Monitoring Service). The SLA (product identifier: SEALEVEL_EUR_PHY_L4_MY_008_068) is an L4 gridded reanalysis product with 0.125° (14 km) spatial resolution computed with respect to a

twenty-year mean (1993–2012). It is estimated by optimal interpolation merging the L3 along-track measurements from different altimeter missions.

The daily SST was obtained from an L4 product (identifier: SST_MED_SSTA_L4_NRT_OBSERVATIONS_010_004) consisting of merged multi-sensor data and optimally interpolated SST fields, also available at CMEMS. The data is provided at 0.0083° (<1 km) spatial resolution and is representative of night-time SST values (00:00 UTC), the so-called foundation SST, nearly free of diurnal warming.

Hourly surface currents measured by HFR with a spatial resolution of approximately 1.5 km were obtained from Puertos del Estado for the 2016–2020 period. In-situ hourly current records were also obtained from ADCPS (TRDI Workhorse 600 kHz and Sentinel V 500 kHz) deployed near the bed at 2 stations on the inner shelf in water depths of 20–23m (see Armona and Cacela, green triangles in Fig. 1).

3.3. Processing

ASCAT records with detected rain and wind speed less than 2 m s^{-1} were discarded due to imprecisions of the sensor under these conditions (KNMI, 2007). The ADCP velocities were depth-averaged after a thorough quality check (for details, see Garel et al., 2016). Likewise, for details on the HFR data processing (i.e. verification of gaps, interpolation, and data validation) see de Oliveira Júnior et al. (2022). Throughout the text, alongshore currents refer to the component parallel to the coast, with positive (negative) values being equatorward (poleward). To remove high-frequency oscillations, the datasets (wind, SST, SLA and currents) were low-pass filtered using a Butterworth filter with a 7-day cut-off period. This cut-off period removes wind fluctuations that are shorter than the 3–4 days period of significant current-driven temperature changes observed in the region (for example, see Figs. 3c and 8c in Garel et al., 2016). The seasonal analysis was performed for each season (with winter: 1 December–28 February; spring: 1 March–31 May; summer: 1 June–31 August; and autumn: 1 September–30 November). The calculation of each seasonal standard deviation (STD) was performed considering the mean value of each individual season.

3.4. Quantification of Ekman transport and Ekman Pumping

The Ekman theory considers that the ocean is submitted to a constant wind and that the only forces acting are the frictional stresses between layers and Coriolis. This assumption corresponds to a linear, homogenous ocean in a steady state, with no lateral gradients and a laterally infinite domain (Bakun, 1973; Simpson and Sharples, 2012). For these conditions, using a locally valid Cartesian coordinate system with x, y, and z aligned eastward, northward, and upward, respectively, and with the corresponding fluid velocity components denoted by u, v, and w, respectively, the equations of motion are:

$$\mathrm{fu} = \frac{1}{\rho}\frac{\partial \tau_y}{\partial z}, \mathrm{fv} = -\frac{1}{\rho}\frac{\partial \tau_x}{\partial z} \mathrm{fv} = -\frac{1}{\rho}\frac{\partial \tau_x}{\partial z} \quad (1)$$

where f is the Coriolis parameter, ρ is the density of seawater and τ_x and τ_y represent wind stresses in the eastward and northward directions, respectively, with:

$$\tau_x = \rho_a \mathrm{Cd} |V_a| u_a \quad (2)$$

$$\tau_y = \rho_a \mathrm{Cd} |V_a| v_a \quad (3)$$

$V_a = (u_a, v_a)$ represents the wind speed vector, ρ_a the air density and Cd a wind stress drag coefficient based on Large and Pond (1981) modified for low wind speeds as in Trenberth et al. (1990):

$$\mathrm{Cd} = 0.00218 \text{ for } |V_a| \leq 1 \text{ m.s}^{-1}$$

$$\mathrm{Cd} = \left(0.62 + 1.56 |V_a|^{-1}\right) 0.001 \text{ for } 1 \text{ m.s}^{-1} < |V_a| < 3 \text{ m.s}^{-1}$$

$$\mathrm{Cd} = 0.00114 \text{ for } 3 \text{ m.s}^{-1} \leq |V_a| < 10 \text{ m.s}^{-1}$$

$$\mathrm{Cd} = (0.49 + 0.065 |V_a|)\, 0.001 \text{ for } |V_a| \geq 10 \text{ m.s}^{-1}$$

Integrating Eq. (1) over the Ekman depth (i.e., where the surface stress is acting significantly) results in relationships for the northward and eastward volume transports per width unit called the Ekman transport $\overrightarrow{\mathrm{Ek_T}} = (\mathrm{Ek}_{Tx}, \mathrm{Ek}_{Ty}$; units of $\mathrm{m}^2.\mathrm{s}^{-1})$ as a function of the eastward and northward surface wind stress, respectively:

$$\mathrm{Ek}_{Tx} = \frac{\tau_y}{\rho f}, \mathrm{Ek}_{Ty} = -\frac{\tau_x}{\rho f} \quad (4)$$

Eq. (4) predicts an integrated transport directed 90° to the right (left) of the surface wind stress in the northern (southern) hemisphere with the coast on the left. For winds parallel to the coast, offshore (onshore) Ekman transport results in cross-shelf mass flux divergence (convergence) that must be compensated by an upward (downward) mass flux. Thus, the cross-shore wind-driven Ekman transport is equal to the vertical transport into the Ekman layer (ignoring any associated sea surface height changes).

In the present study the upwelling intensity due to the coastal upwelling was calculated at every grid node along the 50 m isobath (Fig. 1 black circles) from Eq. (4) using the meridional component of the wind Ek_{Ty} (due the broadly east-west orientation of the coastline and shelf break) and ρ = 1025 kg.m-3. The computation implicitly assumes that 50m is deep enough so that surface and bottom Ekman layers do not overlap.

Divergence (convergence) can also occur in the coastal regions independently of the coastal boundary under a spatially heterogeneous wind field, that generates vertical velocities, called Ekman pumping velocities (w_{Ek} in m.s^{-1}), that are proportional to the wind stress curl:

$$w_{Ek} = \hat{\mathrm{k}} \bullet \left(\frac{1}{\rho f}\right) \nabla \times \vec{\tau} = \left(\frac{1}{\rho f}\right)\left(\frac{\partial \tau_y}{\partial x} - \frac{\partial \tau_x}{\partial y}\right) \quad (5)$$

The upwelling intensity due to the pumping mechanism was estimated by converting w_{Ek} to Ekman pumping transport ($\mathrm{EkP_T}$ in $\mathrm{m}^2.\mathrm{s}^{-1}$) following Pickett (2003). w_{Ek} was integrated from the latitude corresponding to the 50 m isobath to a selected offshore limit at 36°48′N that corresponds to the shelf slope (Fig. 1, red dots) and roughly to the offshore limit of the cold water signal along the NMGoC during the upwelling season (see Vargas et al., 2003). Following the Cartesian coordinate system, positive values of $\mathrm{EkP_T}$ represent downwelling favourable conditions, while positive $\mathrm{EkP_T}$ represent upwelling favourable conditions. For simplification, Ek_{Ty} is multiplied by −1 (such as positive values represent upwelling conditions as $\mathrm{EkP_T}$). Finally, the total alongshore upwelling intensity (or total transport per width unit) was calculated as the sum of Ek_{Ty} and $\mathrm{EkP_T}$, both evaluated along the shelf region between 9°W and 7°W.

4. Results

4.1. Upwelling and downwelling favourable conditions

The variability of the low-pass filtered wind over the NMGoC is briefly described in this section to aid the visualization of the seasonal wind variation and the typical conditions for upwelling and downwelling events associated with Ekman transport and Ekman pumping mechanisms. The seasonal wind roses presented in Fig. 4 show the clear year-round dominance of the winds from the north (mostly from 300° to 360°) over the western bight of the NMGoC. Eastward, the dominant wind direction is generally from west-northwest. The most distinct seasonal patterns are observed between winter and summer (Fig. 4a and c). In summer, at west of 9°W, winds are from the north and often >7.5

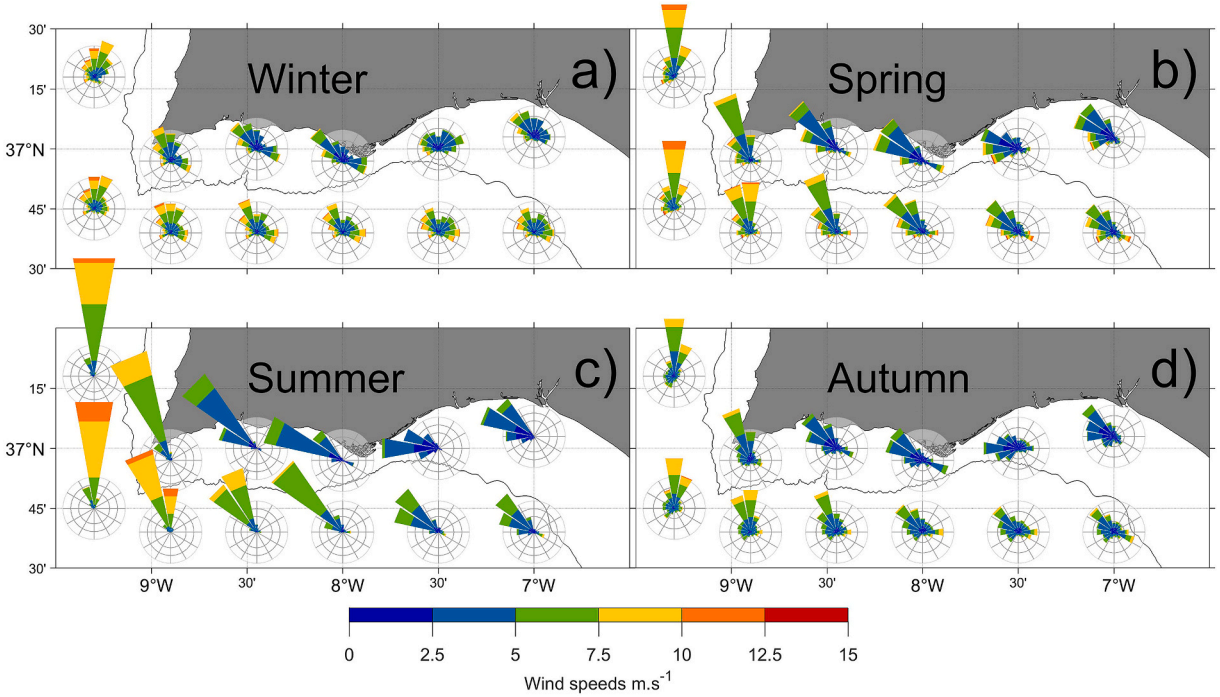

Fig. 4. Seasonal wind roses from the hourly SKIRON modelled data (low pass filtered at 40h), represented with the meteorological convention (i.e. wind provenance). Circles represent 5%, 10% and 20% of occurrences.

m s^{-1}, responsible for strong and persistent upwelling over the Portuguese west coast, while east of 9°W the dominant northerly rotates anticlockwise and weakens importantly. Such an inhomogeneous wind field promotes upwelling due to the pumping mechanism independent of the coastline orientation. An example of a typical summer day with highly heterogeneous wind is presented in Fig. 5a. The variability of wind magnitude and direction near CSV and east of Cape Santa Maria creates a positive and negative wind stress curl, respectively (Fig. 5d). It

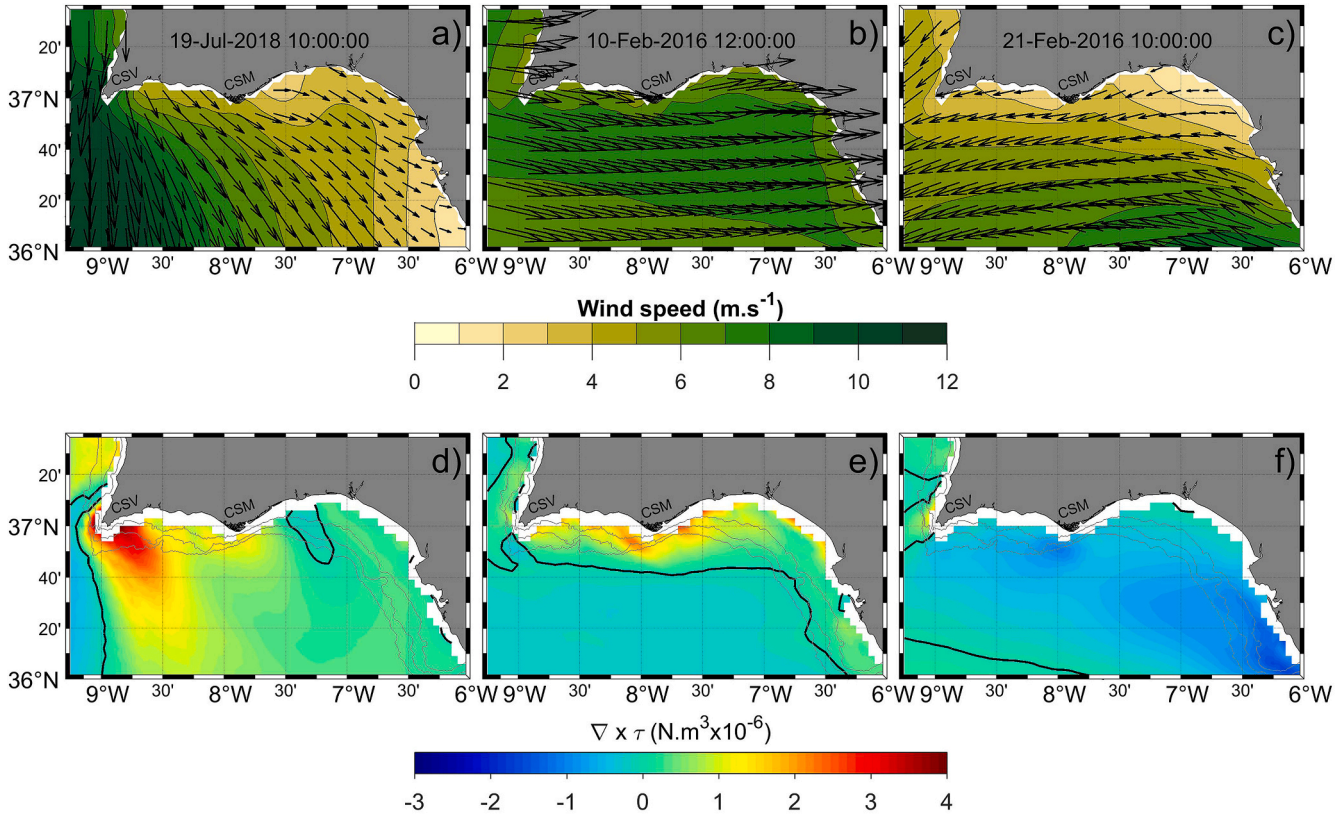

Fig. 5. Upwelling and downwelling favourable conditions from low-pass-filtered SKIRON modelled wind data (top) and the associated wind stress curl magnitude (bottom). Positive (negative) values in red (blue) represent upwelling (downwelling) patterns. Black line in d, e and f represent the 0 wind stress curl.

is also noted that in summer easterlies are rare.

In winter (Fig. 4a), wind directions are the most variable, with velocities often above 5 m s^{-1} along the NMGoC. Easterlies (Levanter) at the NMGoC (e.g., Fig. 5b), occur more often in winter than during the other seasons and promote downwelling conditions through onshore $\overline{Ek_T}$ and negative wind stress curl that is generally moderate along the coast (Fig. 5e). Despite some overall variability in winter, winds from the north quadrant largely prevail over the western region.

Also relevant for this study are the events associated with westerlies, parallel to the coast (as exemplified in Fig. 5c), that promote significant upwelling through offshore $\overline{Ek_T}$. Strong westerly events generally occur in winter and spring (Fig. 4a and b). The associated wind stress curl is generally weak and is confined to a narrow band along the coastal region (e.g., Fig. 5f). In summer and autumn, the western component is dominant, although weak (Fig. 4c and d), and prolonged events may also be important to promote coastal upwelling through offshore $\overline{Ek_T}$.

4.2. Patterns of the $\overline{Ek_T}$

The overall pattern of the $\overline{Ek_T}$ at the NMGoC is defined by westward transport in regions west of 8°W that veer to the south or southwestward at east (Fig. 6a–d). This pattern is modulated seasonally, with westward transport in the western region being strongest during spring and summer (Fig. 6b and c) and weakest in winter and autumn (Fig. 6a and d). The region with the strongest westward mean summer transport is in the vicinity of CSV with values $\geq$ 0.9 $m^3\ s^{-1}.m^{-1}$ (red contours in Fig. 6c). At this location (approximately at 9°W 37°N), the shelf is narrow, and the slope is oriented in the NS direction, indicating that significant upwelling takes place at this region of maximum offshore transport. Strong upwelling also extends further south of CSV due to the magnitude of divergence in transport. For instance, $\overline{Ek_T}$ differences about 0.3–0.5 $m^3\ s^{-1}.m^{-1}$ exists between 8°30′W 36°50′N and 9°W 36°50′N, which are less than 25 km apart.

Compared to the CSV region, the magnitude of the $\overline{Ek_T}$ is generally weak year-round in the eastern region, especially over the shelf where the mean transport is typically below 0.3 $m^3\ s^{-1}.m^{-1}$. However, this weak transport is broadly in the cross-shore direction, thus upwelling favourable, along the entire coast.

4.3. w_{Ek} patterns

Along the shelf w_{Ek} are mostly weak and positive (upward), except for a small region around 7°30′W, with weakly negative values, and the region near CSV, with the strongest positive values (Fig. 6e–h). w_{Ek} near CSV are strongest in spring and summer with maximum values >1x10^{-5} m s^{-1} and >1.5x10^{-5} m s^{-1} respectively (Fig. 6f and g). This upwelling centre is skewed in the eastward direction, indicating that curl-driven upwelling will be more important along the southern than the western Portuguese coast. Offshore, w_{Ek} are generally positive and weak, except at the south-eastern region which is marked by permanent weak

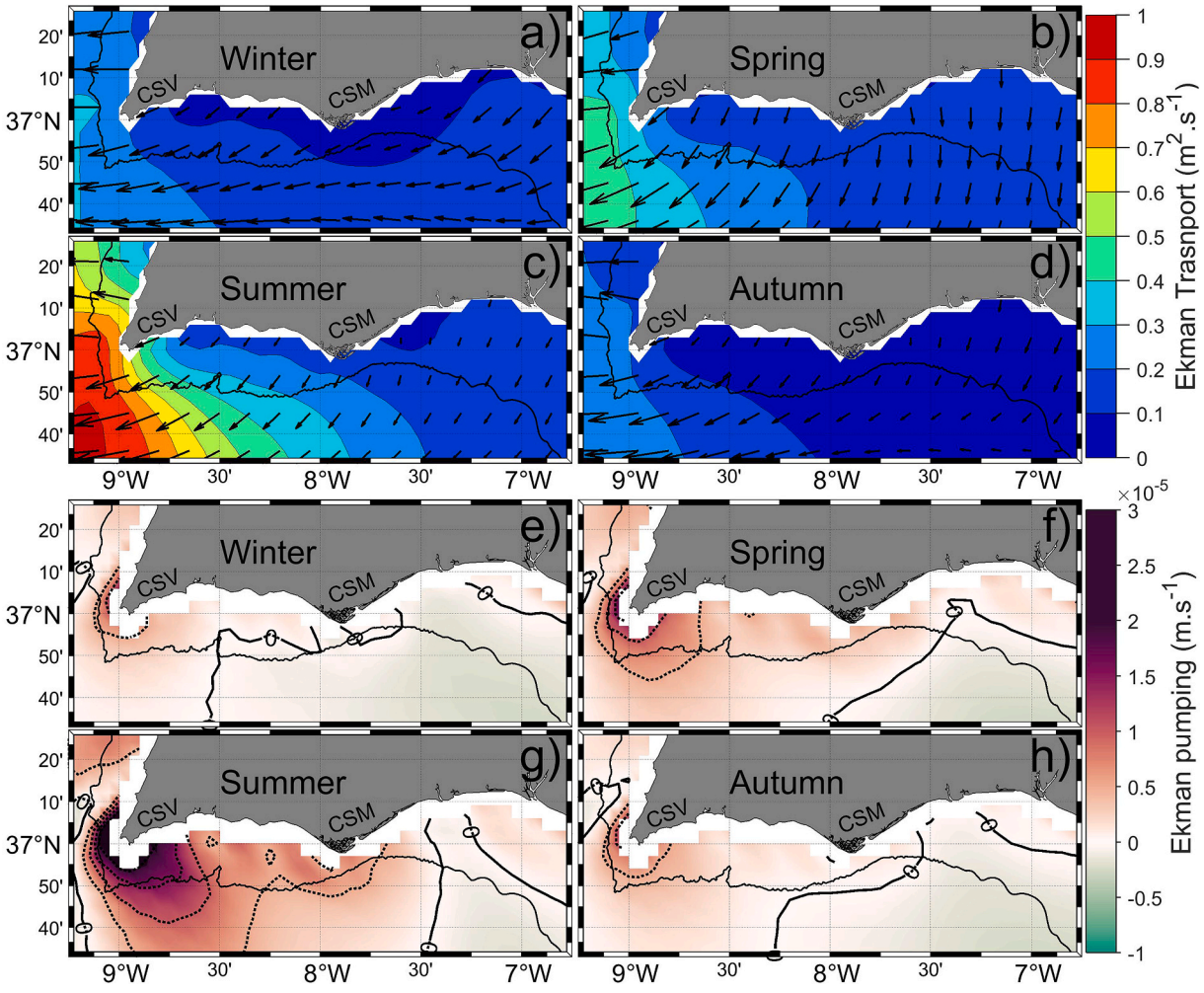

Fig. 6. Seasonal $\overline{Ek_T}$ (a–d) and w_{Ek} (e–h). Doted contours and solid black contour in e-h represent 0.5x10-5 m s^{-1} intervals and zero line respectively. Note that w_{Ek} velocities arise form divergence (convergence) of the $\overline{Ek_T}$. Therefore, regions of strong w_{Ek} coincides with regions of strong Ek_T gradient.

negative (downward velocities) in all seasons.

4.4. Alongshore variability of upwelling intensity

To assess the seasonal variability of the contributions from both Ek_T and EkP_T mechanisms to the total upwelling intensity over the shelf, these parameters are plotted alongshore for each season in Fig. 7. Ek_T is twice stronger in spring and summer (about 0.2 $m^3\ s^{-1}.m^{-1}$) than in autumn and winter (Fig. 7a). Although the $\overline{Ek_T}$ magnitudes in spring and summer are largest at west (Fig. 6b and c), Ek_{Ty} remains spatially constant as the wind becomes increasingly parallel to the coast eastward (see Fig. 4b and c). The Ek_{Ty} standard deviation STD is evenly distributed along the coast with the highest values observed in spring and winter (approximately 0.4 $m^3\ s^{-1}.m^{-1}$) and lowest in summer ($\leq$0.2 $m^3\ s^{-1}.m^{-1}$, Fig. 7b).

The low Ek_{Ty} STD in summer is explained by the steady wind pattern over the region that causes persistent and relatively weak (generally $<$0.5 $m^3\ s^{-1}.m^{-1}$) upwelling favourable conditions sometimes lasting more than a month (see blue in Fig. 8 from the end of June to the end of July 2018). These periods are eventually interrupted by transient easterlies events that last around four days (i.e., 20 June,August 3, 2018 and 20 August in Fig. 8a). The relatively high values of STD in winter and spring are due to the alternation of events with strong (often $>$0.5 $m^3\ s^{-1}.m^{-1}$) upwelling and downwelling favourable conditions (See Fig. 9a). It is noted that the duration of downwelling events remains about four days.

EkP_T is strongest in summer and weakest in winter (Fig. 7c). In all seasons, the highest values are observed near CSV, between 8°30′W and 9°W, and the lowest (broadly negative) values are observed east of 7°30′W. The maximum values (Fig. 7c in red) are 0.5 $m^3\ s^{-1}.m^{-1}$, 2.5 times larger than the concurrent Ek_T. In this region near CSV, summer events are generally strong and often reach values $>$ 0.75 $m^3\ s^{-1}.m^{-1}$ (see Fig. 8b) supporting the dominant contribution from this mechanism to local upwelling. The overall low EkP_T STD values express low variability in time and along the coast. In winter, despite the alternation between upwelling and downwelling favourable conditions, EkP_T values are generally weak (often $<$0.25 $m^3\ s^{-1}.m^{-1}$ see Fig. 9b) along with STD values; in summer, the persistent wind conditions result in low STD values, as for Ek_{Ty}) (see Fig. 8b).

The combined effects of Ek_{Ty} and EkP_T result in upwelling favourable conditions along the entire coast except in winter between 7°15′W and 8°W (Fig. 7e) where the transport is negligible. Although the total transport is the weakest in winter, it also results from the alternation of relatively strong positive and negative events (Fig. 9c). Overall, the NMGoC has year-round coastal upwelling favourable conditions that are strongest near CSV, with total transport often reaching 1 $m^3\ s^{-1}.m^{-1}$ in summer (Fig. 9c) due to a strong EkP_T contribution. The overall sharp decrease of EkP_T eastward of 8°30′W results in an alongshore gradient of the total upwelling intensity that is steepest in summer and smoothest in winter.

5. Effect of coastal upwelling and Ekman pumping on the circulation

5.1. Shelf circulation

To evaluate the effect of Ek_{Ty} and EkP_T on the alongshore shelf circulation, the total transport is compared with SST, alongshore currents

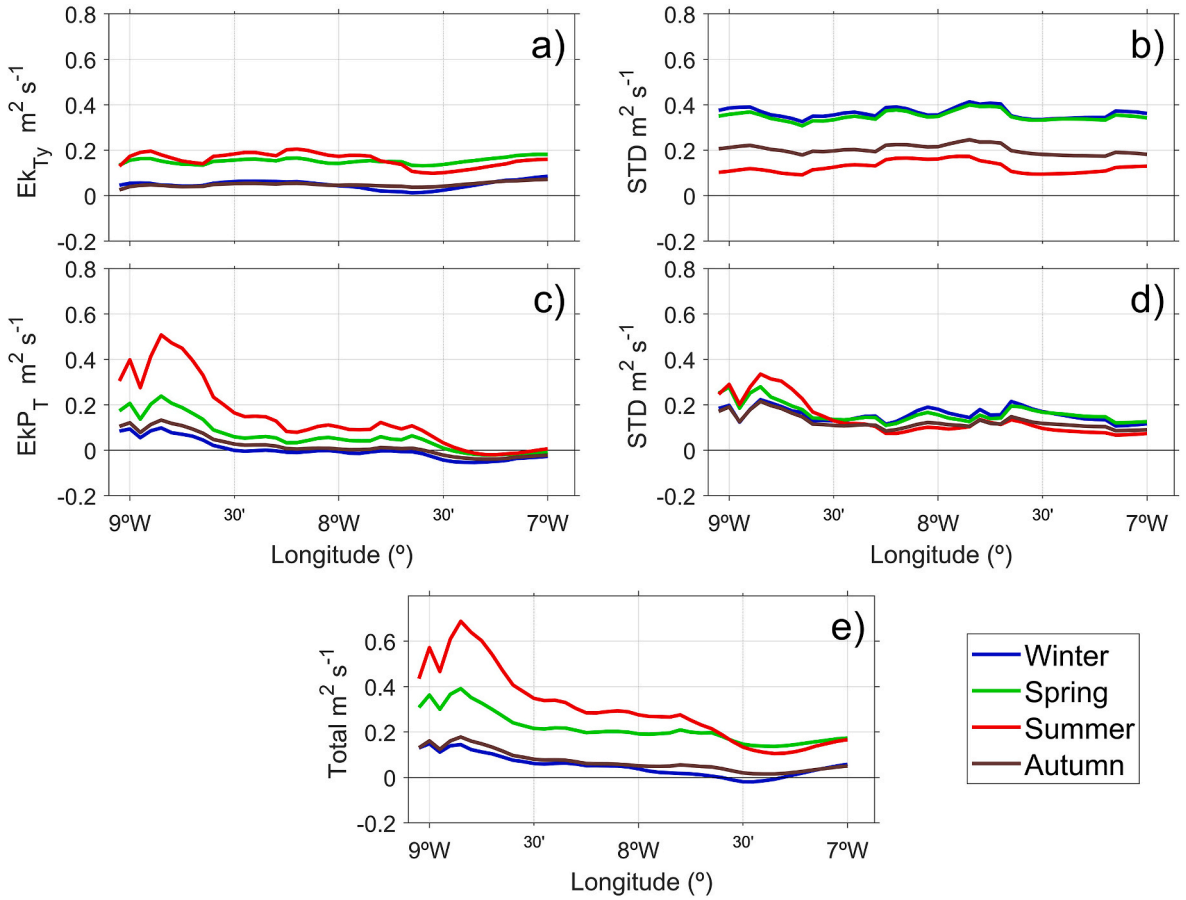

Fig. 7. Seasonal estimates of wind-driven alongshore upwelling intensity due to $\boldsymbol{Ek_{Ty}}$ (a) and $\boldsymbol{EkP_T}$ (c). Seasonal Total transport (e) and modulus of the STD from $\boldsymbol{Ek_{Ty}}$ and $\boldsymbol{EkP_T}$ (b and d respectively).

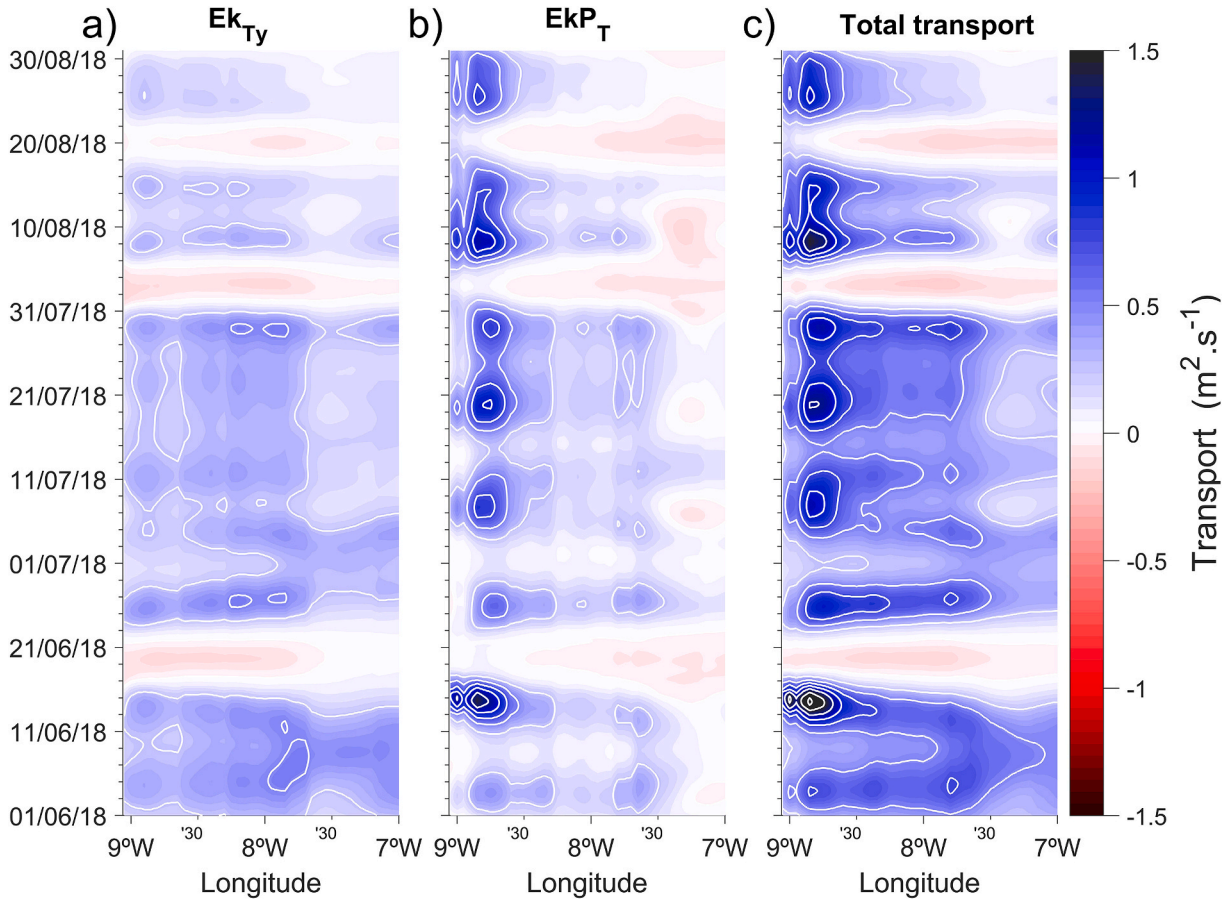

Fig. 8. Time variability of $\boldsymbol{Ek_{Ty}}$ (a), $\boldsymbol{EkP_T}$ (b) and Total transport (c) during the summer of 2018. Upwelling (downwelling) favourable conditions are represented in blue (red). Contours indicate 0.25 $m^3\ s^{-1}.m^{-1}$ intervals and minor ticks indicate 2-day intervals.

from HFR and ADCP, and SLA considering a 5-month period, from May to September 2019 (Fig. 10). The selected period includes events with significant wind stress curl near CSV that produce an alongshore gradient in the total transport and events with upwelling favourable conditions evenly distributed along the coast (reflecting the effect of Ek_{Ty}). In general, when upwelling favourable events (blue in Fig. 10) with moderate magnitude ($<1\ m^3\ s^{-1}.m^{-1}$) are observed along the entire coast, SST cooling is also observed over the corresponding area (see events on 08 May, 18 May and 7 July, blue arrows in Fig. 10b). By contrast, periods with strong upwelling favourable conditions restricted to the CSV region are associated with localized SST cooling, mostly at west of 8°W (see events on 18 July, 02 August and 17 August, red arrows in Fig. 10b). These patterns depict a strong control of the coastal SST by the intensity and alongshore extent of upwelling favourable conditions. Upwelling favourable westerlies are typically associated with an equatorward circulation at the NMGoC that prevents or hampers the westward progression of the pool of warm water from the eastern region (García Lafuente and Ruiz, 2007). Multi-year statistical analyses of SST presented by Vargas et al. (2003) have shown that in winter cold waters are found stretching along the entire shelf, following the strong and evenly distributed positive Ek_{Ty} along the coast (Fig. 9a). Their results also indicate that in summer the coldest coastal waters are observed over the western bight and extend further south over the slope, following closely the pattern of w_{Ek} (Fig. 6g). Towards the east, w_{Ek} tends towards zero at 7°30W in spring and summer (Fig. 6f and g), resulting in a weak total upwelling intensity eastward of this location (Fig. 7e). This specific position also delimits the extent of negative SST anomalies (Vargas et al., 2003) and the area with a probability of finding upwelling spots based on remotely sensed chlorophyll and SST (Ruiz and Navarro, 2006). Overall, the spatial and temporal correspondences between the SST and upwelling intensity support that both coastal upwelling and Ekman pumping affect importantly the shelf water circulation throughout the year.

Long-term in-situ observations at Armona station clearly show that coastal equatorward flows are driven by westerlies that promote upwelling (de Oliveira Júnior et al., 2021). In agreement, upwelling favourable conditions (blue in Fig. 10a) are associated with equatorward flows (positive values in Fig. 10c) during Period 1. On the contrary, the development of poleward flows (negative values in Fig. 10c) was mainly associated with weak total transport at the eastern bight (white, Fig. 10a) and with persistent and strong upwelling favourable conditions at the western bight (see the events indicated by black arrows in Fig. 10c, except the first event in early June) confirming that these flows are not triggered by direct favourable wind action (Garel et al., 2016). In most of these well-established events (highlighted with arrows in Fig. 10c), poleward flow reversals were associated with an SLA slope positive eastward (Fig. 10d) that is compatible with upwelling restricted to the western bight. During these events, SLA variations reach up to 4 cm for a distance of approximately 110 km along the coast (between 7°30′W and 8°30′W), similar to estimates from tide gauges between the eastern and western bights (Relvas and Barton, 2002). In addition, such slope if acting alone on the flow (i.e., ignoring all the other terms of the momentum equation), produces a poleward acceleration of $3.6x10^{-6}$ m s^{-2} that is of the same order of magnitude as the acceleration during poleward flow reversals at Armona station (de Oliveira Júnior et al., 2021), consistent with poleward CCCs driven by an alongshore pressure gradient (de Oliveira Júnior et al., 2021; García-Lafuente et al., 2006; Garel et al., 2016; Relvas and Barton, 2002; Sánchez et al., 2006). The correspondence between the SLA alongshore gradient and the

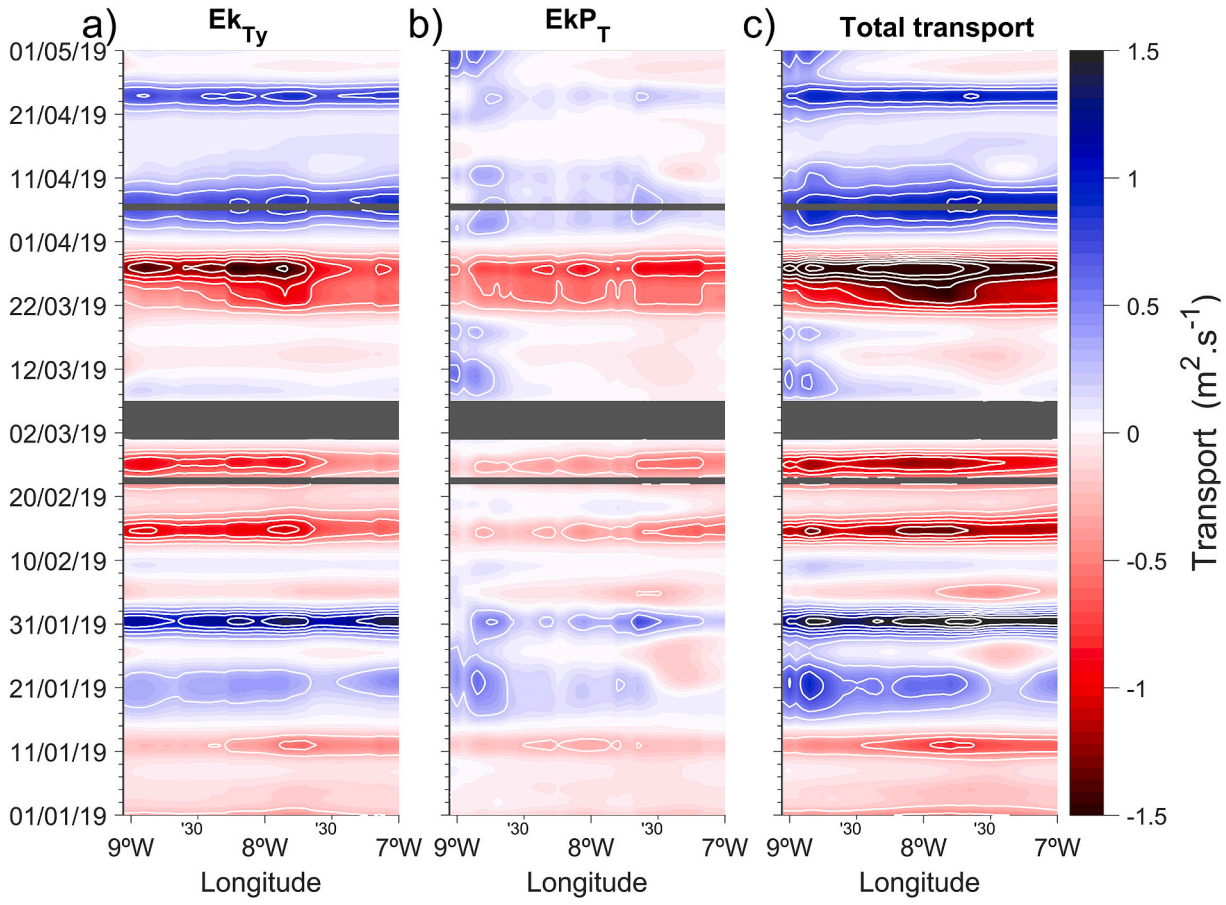

Fig. 9. Same as in Fig. 8 but for the winter of 2019.

alongshore gradient of total transport, which is largely dominated by the EkP$_T$ in summer (Fig. 7), suggests that the pressure gradient is partly produced by the wind stress curl, as proposed by Sánchez et al. (2006). Numerical simulations in the Santa Barbara Channel have shown that the alongshore gradient of wind stress curl is an essential factor in producing an alongshore pressure gradient and, consequently, poleward flows (Oey, 1999; Oey et al., 2001; Wang, 1997). It is important to stress that additional factors than the wind stress curl may also generate an alongshore pressure gradient. For instance, a pressure gradient may develop along the NMGoC due to buoyancy inputs at the eastern bight (Bellanco and Sánchez-Leal, 2016) resulting from the tidal pumping of water warmed up within large intertidal areas in summer (García-Lafuente et al., 2006) and from high river discharge events in winter (Sánchez et al., 2006). The interaction of the upwelling jet generated at the Portuguese west coast with CSV may also affect the sea level. At the Californian coast, equatorward flows produce negative alongshore pressure gradients and accelerate poleward coastal currents when upwelling favourable winds relax (Gan and Allen, 2002).

During Period 2 (from 21 August onwards in Fig. 10), the total transport was weak and varied between upwelling and downwelling conditions. The magnitude of poleward currents was low (<0.1 m s^{-1}), except near CSV (>0.2 m s^{-1}, black solid line in Fig. 10c), where it was comparable to the situation during the well-developed downwelling events on 14 May and 01 June during period 1. The current magnitude difference between the western (black and green solid lines in Fig. 10c) and eastern bights (magenta and red solid lines and dashed black line in Fig. 10c) during the period from 29 August to 08 September, corresponds to a westward shift of the maximum alongshore pressure gradient, being significant only over the western region between 8°49′W and 8°10′W (see black arrow in Fig. 10d). This propagation of the sea level slope is consistent with continental shelf-wave dynamics for which a pressure perturbation propagates poleward along an isobath (Gill, 1982). The strong and localized effect of wind stress curl near CSV may, therefore, trigger the generation of a coastal trapped wave (e.g. Kelvin wave), as suggested by Sánchez et al. (2006) and influences the circulation further north along the Portuguese west coast.

At the western bight, a cyclonic circulation cell is recurrently observed at the water surface with HFR data when the wind relaxes (de Oliveira Júnior et al., 2022). Occasional in-situ measurements have shown that this structure can extend up to 300 m in depth (García-Lafuente et al., 2006). The progressing geostrophic adjustment to the uprise of isopycnals in a circular shape by positive w_{Ek} is expected to induce a cyclonic circulation (Criado-Aldeanueva et al., 2006) as observed at the Santa Barbara Channel (Di Lorenzo, 2003; Münchow, 2000). At the NMGoC, a permanent circular depression in the seasonal SLA (Fig. 11) corresponds remarkably to the spatial and temporal patterns of the positive w_{Ek} (Fig. 6), especially in summer (Figs. 11c and 6g). This depression produces a permanent alongshore slope along the entire NMGoC and a cross-shore-slope over the western bight. Further evidence of the wind stress curl effect on the mesoscale pressure field is provided by the dynamic topography computed near CSV during a synoptic survey in summer (Fig. 5d in Relvas and Barton, 2005). This survey reports a similar circular depression in the sea level at the western bight, marked by a sharp alongshore gradient at 8°30W, where the gradient of Ekman pumping is also the strongest (see Figs. 6 and 7). Therefore, it is proposed that, similar to the Santa Barbara Channel, a cyclonic circulation is produced over the western bight of the NMGoC by isopycnals rising in response to the wind curl.

5.2. GCC modulation

A recent study based on 4.5-year HFR data showed that the slope

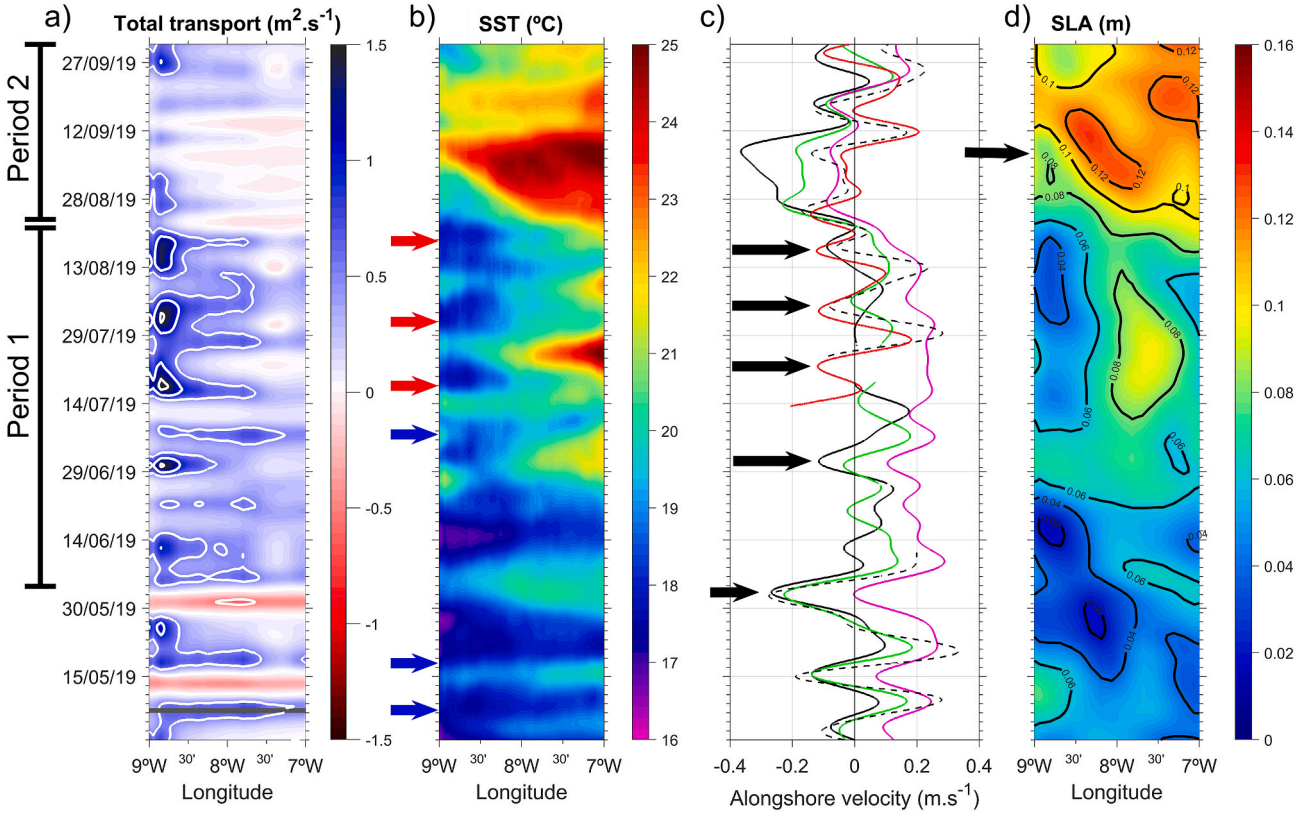

Fig. 10. (a) Hovmöller diagram for the Total transport (Ek_{Ty} + EkP_T). White contours represent 0.5 m^3 s^{-1}.m^{-1} intervals. (b) Hovmöller diagram for the SST averaged from the coast to the 36°48′N line that broadly represents the shelf break limit. Blue and red arrows represent different upwelling responses to the eastward extent of total transport. (c) Surface alongshore currents from HFR near CSV (HFR 1, black solid line), near 8°30′W (HFR2, green solid line) and at Cape Santa Maria (HFR3, magenta solid line). Depth-averaged alongshore ADCP currents at Armona (black dashed line) and Cacela (red solid line) stations. For locations of current velocities see Fig. 1. Black arrows in (c) represent well-established poleward flow events. (d) Hovmöller diagram of the SLA at the 36°56′N line. Contours represent 0.02 m intervals. Black arrow represents a specific event of westward propagation of the sea level slope (see text). All data have been lowpass filtered using a (Butterworth) filter of 7 days cutoff period.

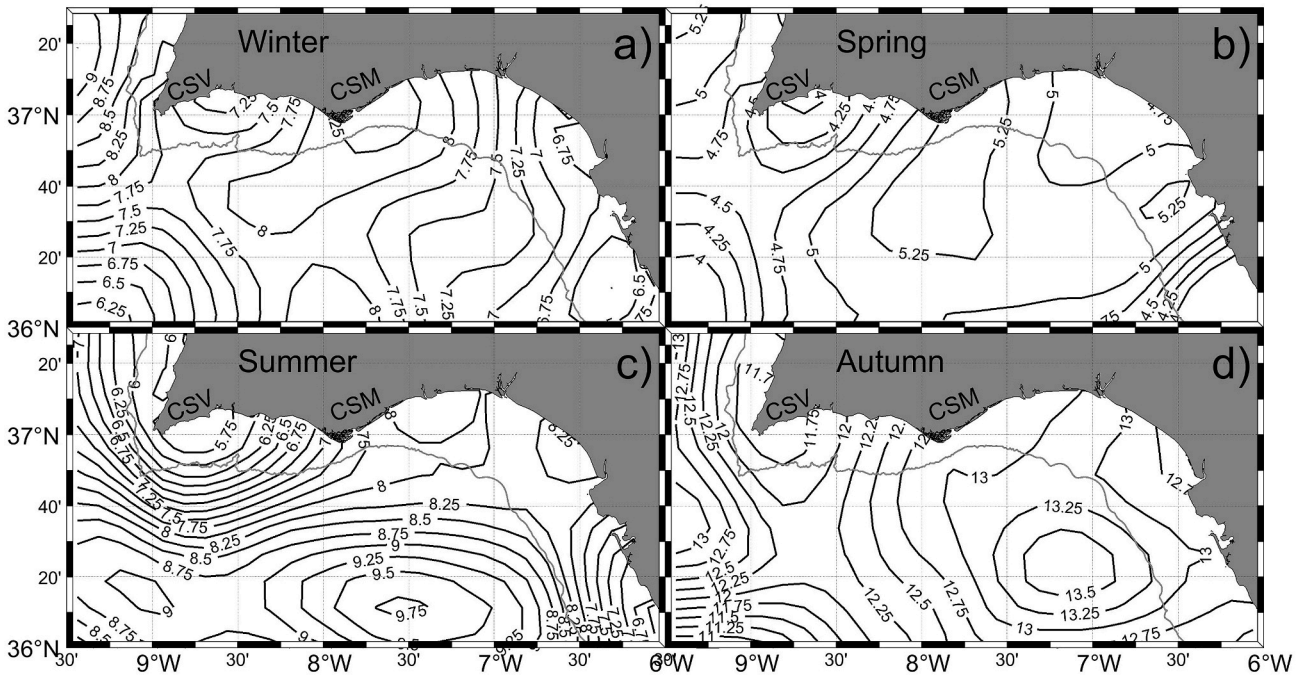

Fig. 11. Seasonal mean SLA. Contour lines represent 0.25 cm intervals.

current, the GCC, is seasonally modulated at the western bight, possibly due to seasonal variability of coastal upwelling and Ekman pumping mechanisms (de Oliveira Júnior et al., 2022). This modulation is observed in the seasonality of the SLA (Fig. 11), with a weak cross-shore pressure gradient over the margin in winter (Fig. 11a) that is significantly enhanced at the slope in summer (Fig. 11c). Owing to the similarities between SLA and w_{Ek} (compare Figs. 11 and 6e–h), the wind stress curl effect may contribute to the modulation of the GCC's position and intensity. Simplified two-dimensional modelling experiments performed to explore the role of wind stress curl in the separation of a coastal upwelling jet along the Oregon coast (Castelao and Barth, 2007) considered two different scenarios, including and omitting the curl effect on the idealized upwelling favourable conditions. It was shown that southward (upwelling favourable) alongshore wind stress intensification and zero curl promote an equatorward jet geostrophically balanced with the tilted isopycnals centred at the shelf break and slope (no separation). Simulations that included wind stress curl intensification, showed that the curl-driven upwelling causes isotherms to tilt upward in the offshore region, thus sustaining an intensification of the southward velocities via the thermal wind balance and controlling the separation of the jet from the slope. To further explore the relationship between the different upwelling mechanisms and the slope circulation, an example containing an offshore migration of the GCC observed from HFR measurements is presented in Fig. 12 together with the spatial and temporal variability of w_{Ek}, SST, Ek_{Ty} and SLA gradient along a cross-shore transect (at 8°30′W, approximately).

From 1 March to 15 May (Period 3 in Fig. 12), the circulation was marked by several events with a well-developed GCC (outlined with black contours in Fig. 12a) close to the 200 m isobath (horizontal black line, indicating the shelf break limit at 30 km from the coast). During this period, w_{Ek} was mostly positive (upwelling favourable) and relatively weak ($<1x10^{-5}$ m s^{-1}, Fig. 12b, filled contours) except a strong negative event in March 2019. Similarly, Ek_{Ty} was mostly positive (upwelling favourable) and two strong events were registered in April (blue arrows in Fig. 12b). The SST (Fig. 12c) was always slightly colder near the coast than offshore, and a moderate negative (higher sea level offshore) SLA gradient ($-0.5x10^{-6}$) was generally observed over the shelf break (Fig. 12d) in agreement with the coastal upwelling mechanism. An exception to this pattern occurred at the end of March due to a strong downwelling (negative w_{Ek} and Ek_{Ty}) event that caused the slope to reverse sign (first offshore on 16th March and, later in April, over the entire shelf) and was associated with a westward current along the entire transect. Overall, the oceanographic features (in terms of alongshore current, SST and cross-shore SLA) at the western NMGoC during Period 3 in Fig. 12, corroborate the theoretical explanation for the development of a typical coastal upwelling circulation. More specifically, when the surface water divergence is restricted to the coastal boundary (due mainly to $Ek_{Ty}Ek_{T}$ and no significant curl), the cross-shore pressure gradient develops close to the coast, and the circulation features a geostrophic upwelling jet over the shelf break (Capet et al., 2004; Castelao and Barth, 2007). Additional evidence that, in winter, strong events of positive Ek_{Ty} and positive w_{Ek} near the coast affect the NMGoC circulation is provided by the recurrently observed upward tilted isopycnals near the coast during winter surveys at the eastern bight (Santos, 2005; Silva et al., 2008). This stratification profile, typical of wind-driven upwelling, contributes to the persistence of the GCC in winter (Criado-Aldeanueva et al., 2009; de Oliveira Júnior et al., 2022).

In the example presented in Fig. 12, the Ekman pumping effect became important during the second half of May (beginning of Period 4 in Fig. 12) with the development of two strong events with $w_{Ek} > 1x10^{-5}$ m s^{-1} (see red arrows in Fig. 12b). These events were closely associated with the steepening and broadening of cross-shore SLA gradient (see black box in Fig. 12d) along with the strengthening and widening of the GCC (Fig. 12a). In the following months up to the end of

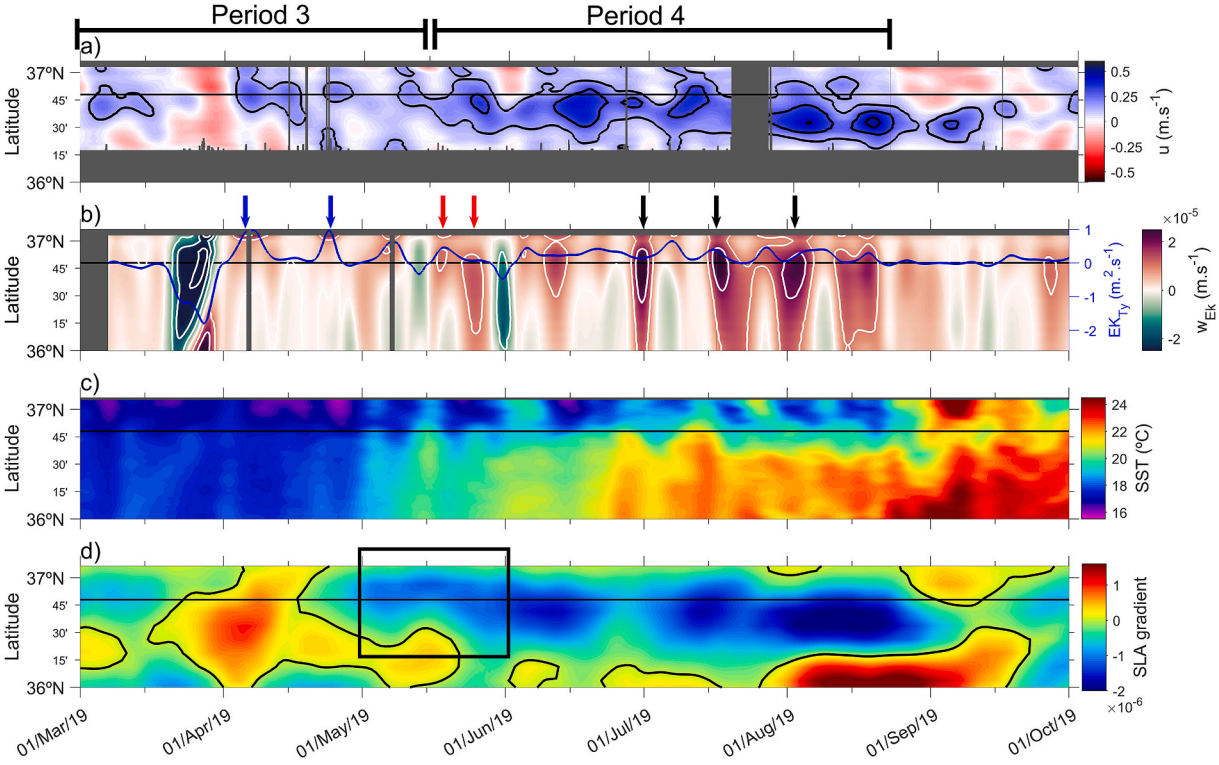

Fig. 12. Hovmöller diagram (spring and summer 2019) for the (a) zonal component of the surface currents from HFR extracted from a cross-shore transect at the western bight, (b) w_{Ek} (filled contours) and Ek_{Ty} (blue line, right axis), (c) SST and (d) cross-shore SLA gradient. All colormaps represent data extracted along a cross-shelf transect near 8°30′W. The contours in (a) represent 0.15 m s^{-1}, 0.3 m.s^{-1}and 0.45 m s^{-1}. The contour interval in (b) is $1x10^{-5}$ m s^{-1} and the contour in (d) represents 0. In all panels, the horizontal black line indicates the 200 m depth, indicative of the shelf break limit that is at 30 km from the coast. On the right axis in (b) this black line also represents the zero Ek_{Ty} transport line. All data have been lowpass filtered using a (Butterworth) filter of 7 days cutoff period.

September, w_{Ek} intensified and reached velocities $> 2x10^{-5}$ m s^{-1} (see black arrows in Fig. 12b) off the shelf break and was associated with an enhancement of the cross-shore SLA gradient which explains the offshore migration (up to 20 km from the shelf break) and strengthening (velocities >0.45 m s^{-1}) of the GCC core. The concurrent flow separation and w_{Ek} intensification, together with the common offshore area with strong w_{Ek} and SLA gradient, support that the GCC at the western bight is affected locally by the wind stress curl effect following the dynamics proposed by Castelao and Barth (2007). Additional processes acting on the GCC include, amongst others, the effect of the west coast upwelling jet that is forced to turn cyclonically due to the conservation of potential vorticity near CSV (Sánchez and Relvas, 2003) and the mixing between the Atlantic water and the Mediterranean outflow over the eastern Gulf of Cadiz (Kida et al., 2008; Peliz et al., 2007, 2009a).

6. Conclusions

Winds from SKIRON, a high-resolution weather forecast model, were used to estimate coastal upwelling and Ekman pumping and explore their effects on the circulation at the NMGoC. Due to the model's high spatial resolution, it was possible to resolve small-scale wind patterns induced by the irregular coastline and coastal topography. In general upwelling favourable conditions occur along the study area. The strongest upwelling intensity occurs near CSV due to a persistent positive wind stress curl that promotes an alongshore gradient of upwelling intensity throughout the year but stronger in summer.

Over the western bight, due to strong coastal upwelling events and comparatively weaker Ekman Pumping (which is maximum over the shelf) in winter, the surface water divergence is restricted to the coastal boundary. Consequently, the development of a cross-shore pressure gradient occurs close to the coast, and the offshore circulation is marked by a geostrophic upwelling jet, the GCC, at the upper slope. In summer, Ekman Pumping intensifies and promotes upwelling in regions beyond the shelf. In response, the sea level gradient extends further offshore and contributes to the GCC separation. Therefore, the seasonal and spatial variability of coastal upwelling and Ekman pumping is shown to contribute significantly to the offshore position of the GCC at the western region.

The permanent and strong effect of Ekman pumping anchored at CSV is argued to sustain an overall circular depression at the sea level over the western bight, as evidenced by satellite altimetry. The dynamic adjustment of this depression may favour the recurrently observed cyclonic circulation in the area that alternates with the dominant eastward circulation. A permanent alongshore pressure gradient, whose magnitude in summer is comparable with tide gauge observations, is also associated with the depression and could effectively drive coastal currents poleward.

Overall, this study indicates that the circulation in the NMGoC is highly affected by the atmosphere-ocean interaction through modulation of the pressure field induced by spatially and temporally variable upwelling processes. Future work should take into consideration how internal and external forcing compare and also the far-field effects that have been ignored in the present study.

CRediT authorship contribution statement

Luciano de Oliveira Júnior: Writing – review & editing, Writing – original draft, Visualization, Methodology, Investigation, Formal analysis, Data curation, Conceptualization. **Paulo Relvas:** Writing – review & editing, Writing – original draft, Supervision, Project administration, Methodology, Investigation, Funding acquisition, Formal analysis, Conceptualization. **Erwan Garel:** Writing – review & editing, Writing – original draft, Supervision, Project administration, Methodology, Investigation, Funding acquisition, Formal analysis, Conceptualization.

Declaration of competing interest

The authors declare that they have no known competing financial interests or personal relationships that could have appeared to influence the work reported in this paper.

Acknowledgements

The authors are thankful for the Helenic National Meteorological Service for kindly supplying SKIRON wind fields. It is also acknowledged CMEMS for providing satellite altimetry and satellite sea surface temperature products (https://marine.copernicus.eu/) and the Remote Sensing Systems (https://remss.com/) for providing ASCAT wind data. The authors additionally thank IPMA in the person of Teresa Drago, and Tunipex for the support with the ADCP deployments and Puertos del Estado for providing high-frequency radar data. LOJ, PR and EG acknowledge the support of the Portuguese Foundation for Science and Technology (FCT) through the grant UID/MAR/00350/2020 attributed to CIMA, University of Algarve (doi 10.54499/UIDB/00350/2020); LA/P/0069/2020 awarded to the Associate Laboratory ARNET (doi 10.54499/LA/P/0069/2020) grants UIDB/04326/2020, UIDP/04326/2020 and LA/P/0101/2020 (attributed to CCMAR); and through the PhD fellowship SFRH/BD/140250/2018 attributed to LOJ.

References

Alvarez, I., Gomez-Gesteira, M., deCastro, M., Dias, J.M., 2008. Spatiotemporal evolution of upwelling regime along the western coast of the Iberian Peninsula. J. Geophys. Res. Ocean. 113 https://doi.org/10.1029/2008JC004744.

Bakun, A., 1973. Coastal upwelling indices, west coast of North America, 1946–1971. NOAA Tech. Rep. NMFS SSFR-671 103. NMFSSSRF-671.

Bellanco, M.J., Sánchez-Leal, R.F., 2016. Spatial distribution and intra-annual variability of water masses on the Eastern Gulf of Cadiz seabed. Cont. Shelf Res. 128, 26–35. https://doi.org/10.1016/j.csr.2016.09.001.

Bravo, L., Ramos, M., Astudillo, O., Dewitte, B., Goubanova, K., 2016. Seasonal variability of the Ekman transport and pumping in the upwelling system off central-northern Chile (~ 30° S) based on a high-resolution atmospheric regional model (WRF). Ocean Sci. 12, 1049–1065. https://doi.org/10.5194/os-12-1049-2016.

Capet, X.J., Marchesiello, P., McWilliams, J.C., 2004. Upwelling response to coastal wind profiles. Geophys. Res. Lett. 31, 1–4. https://doi.org/10.1029/2004GL020123.

Capon, R.A., 2006. High resolution studies of the Gibraltar Levanter validated using sun-glint anemometry. Meteorol. Appl. 13, 257–265. https://doi.org/10.1017/S135048270600226X.

Castelao, R.M., Barth, J.A., 2007. The role of wind stress curl in jet separation at a Cape. J. Phys. Oceanogr. 37 (1), 2652–2671. https://doi.org/10.1175/2007JPO3679.

Castelao, R.M., Barth, J.A., 2006. Upwelling around Cabo Frio, Brazil: the importance of wind stress curl. Geophys. Res. Lett. 33, 2–5. https://doi.org/10.1029/2005GL025182.

Castelao, R.M., Luo, H., 2018. Upwelling jet separation in the California current system. Sci. Rep. 1–8. https://doi.org/10.1038/s41598-018-34401-y.

Chase, J., 1951. The Bermuda-Azores High Pressure Cell; its Surface Wind Circulation. Woods Hole Oceanographic Institution.

Cravo, A., Relvas, P., Cardeira, S., Rita, F., 2013. Nutrient and chlorophyll a transports during an upwelling event in the NW margin of the Gulf of Cadiz. J. Mar. Syst. 128, 208–221. https://doi.org/10.1016/j.jmarsys.2013.05.001.

Criado-Aldeanueva, F., García-Lafuente, J., Navarro, G., Ruiz, J., 2009. Seasonal and interannual variability of the surface circulation in the eastern Gulf of Cadiz (SW Iberia). J. Geophys. Res. 114, C01011 https://doi.org/10.1029/2008JC005069.

Criado-Aldeanueva, F., García-Lafuente, J., Vargas, J.M., Del Río, J., Vázquez, A., Reul, A., Sánchez, A., 2006. Distribution and circulation of water masses in the Gulf of Cadiz from in situ observations. Deep Sea Res. Part II Top. Stud. Oceanogr. 53, 1144–1160. https://doi.org/10.1016/j.dsr2.2006.04.012.

de Oliveira Júnior, L., Garel, E., Relvas, P., 2021. The structure of incipient coastal counter currents in South Portugal as indicator of their forcing agents. J. Mar. Syst. 214, 103486 https://doi.org/10.1016/j.jmarsys.2020.103486.

de Oliveira Júnior, L., Relvas, P., Garel, E., 2022. Kinematics of surface currents at the northern margin of the Gulf of Cádiz. Ocean Sci. 18, 1183–1202. https://doi.org/10.5194/os-18-1183-2022.

Di Lorenzo, E., 2003. Seasonal dynamics of the surface circulation in the southern California current system. Deep. Res. Part II Top. Stud. Oceanogr. 50, 2371–2388. https://doi.org/10.1016/S0967-0645(03)00125-5.

Dorman, C.E., Beardsley, R.C., Limeburner, R., 1995. Winds in the strait of Gibraltar. Q. J. R. Meteorol. Soc. 121, 1903–1921. https://doi.org/10.1002/qj.49712152807.

Fiúza, A.F.G., 1983. Upwelling patterns off Portugal. In: Suess, E., Thiede, J. (Eds.), Coastal Upwelling its Sediment Record. Springer US, Boston, MA, pp. 85–98. https://doi.org/10.1007/978-1-4615-6651-9_5.

Fiúza, A.F.G., de Macedo, M.E., Guerreiro, M.R., 1982. Climatological space and time variation of the Portuguese coastal upwelling. Oceanol. Acta 5, 31–40.

Gan, J., Allen, J.S., 2002. A modeling study of shelf circulation off northern California in the region of the Coastal Ocean Dynamics Experiment: response to relaxation of upwelling winds. J. Geophys. Res. 107, 3123. https://doi.org/10.1029/2000JC000768.

García-Lafuente, J., Delgado, J., Criado-Aldeanueva, F., Bruno, M., del Río, J., Miguel Vargas, J., 2006. Water mass circulation on the continental shelf of the gulf of Cádiz. Deep sea Res. Part II Trop. Stud. Oceanogr. 53, 1182–1197. https://doi.org/10.1016/j.dsr2.2006.04.011.

Garcia, C.M., Prieto, L., Vargas, M., Echevarría, F., Garcia-Lafuente, J., Ruiz, J., Rubin, J. P., 2002. Hydrodynamics and the spatial distribution of plankton and TEP in the gulf of Cadiz (SW Iberian Peninsula). J. Plankton Res. 24, 817–833. https://doi.org/10.1093/plankt/24.8.817.

García Lafuente, J., Ruiz, J., 2007. The Gulf of Cádiz pelagic ecosystem: a review. Prog. Oceanogr. 74, 228–251. https://doi.org/10.1016/j.pocean.2007.04.001.

Garel, E., Laiz, I., Drago, T., Relvas, P., 2016. Characterisation of coastal counter-currents on the inner shelf of the Gulf of Cadiz. J. Mar. Syst. 155, 19–34. https://doi.org/10.1016/j.jmarsys.2015.11.001.

Gill, A.E., 1982. Atmosphere-Ocean Dynamics. Academic Pess, New York, pp. 319–322.

Hoinka, K.P., De Castro, M., 2003. The Iberian Peninsula thermal low. Q. J. R. Meteorol. Soc. 129, 1491–1511. https://doi.org/10.1256/qj.01.189.

Janjic, Z.I., Gerrity, J., Nickovic, S., 2001. An alternative approach to nonhydrostatic modeling. Mon. Weather Rev. 129, 1164–1178. https://doi.org/10.1175/1520-0493(2001)129<1164:AAATNM>2.0.CO;2.

Jayaram, C., Jose, F., 2022. Relative dominance of wind stress curl and Ekman transport on coastal upwelling during summer monsoon in the southeastern Arabian Sea. Cont. Shelf Res. 244, 104782 https://doi.org/10.1016/j.csr.2022.104782.

Kallos, G., Papadopoulos, A., Katsafados, P., Nickovic, S., 2006. Transatlantic Saharan dust transport: model simulation and results. J. Geophys. Res. Atmos. 111, 1–11. https://doi.org/10.1029/2005JD006207.

Kida, S., Price, J.F., Yang, J., 2008. The upper-oceanic response to overflows: a mechanism for the Azores current. J. Phys. Oceanogr. 38 (1), 880–895. https://doi.org/10.1175/2007JPO3750.

KNMI, 2007. ASCAT Wind Product User Manual.

Large, W.G., Pond, S., 1981. Open Ocean momentum flux measurements in moderate to strong winds. J. Phys. Oceanogr. 11, 324–336. https://doi.org/10.1175/1520-0485(1981)011<0324:OOMFMI>2.0.CO;2.

Losada, A.M.P., 1999. Analysis of the meteorological synoptic situations that affect the Straits of Gibraltar and their influence on the surface wind. Bol. Inst. Esp. Ocean. 15, 81–90.

Mazé, J.P., Arhan, M., Mercier, H., 1997. Volume budget of the eastern boundary layer off the Iberian Peninsula. Deep-Sea Res. Part I Oceanogr. Res. Pap. 44, 1543–1574. https://doi.org/10.1016/S0967-0637(97)00038-1.

Münchow, A., 2000. Wind stress curl forcing of the coastal ocean near Point Conception, California. J. Phys. Oceanogr. 30, 1265–1280. https://doi.org/10.1175/1520-0485(2000)030<1265:WSCFOT>2.0.CO;2.

Oey, L.-Y., 1999. A forcing mechanism for the poleward flow off the southern California coast. J. Geophys. Res. 104, 13529–13539. https://doi.org/10.1029/1999JC900066.

Oey, L.-Y., 1996. Flow around a coastal bend: a model of the Santa Barbara Channel eddy. J. Geophys. Res. 101, 16667–16682. https://doi.org/10.1029/96JC01232.

Oey, L.-Y., Wang, D.-P., Hayward, T., Winant, C., Hendershott, M., 2001. "Upwelling" and "cyclonic" regimes of the near-surface circulation in the Santa Barbara Channel. J. Geophys. Res. Ocean. 106, 9213–9222. https://doi.org/10.1029/1999JC000129.

Papadopoulos, A., Katsafados, P., Kallos, G., Nickovic, S., 2002. The weather forecasting system for POSEIDON - an overview. Glob. Atmos. Ocean Syst. 8, 219–237. https://doi.org/10.1080/10236730290000003543.

Peliz, A., Boutov, D., Barbosa Aguiar, A., Carton, X., 2014. The gulf of Cadiz gap wind anticyclones. Cont. Shelf Res. 91, 171–191. https://doi.org/10.1016/j.csr.2014.09.004.

Peliz, A., Dubert, J., Marchesiello, P., Teles-Machado, A., 2007. Surface circulation in the Gulf of Cadiz: model and mean flow structure. J. Geophys. Res. 112, C11015 https://doi.org/10.1029/2007JC004159.

Peliz, A., Marchesiello, P., Santos, A.M.P., Dubert, J., Teles-Machado, A., Marta-Almeida, M., Le Cann, B., 2009a. Surface circulation in the gulf of Cadiz: 2. Inflow-Outflow coupling and the gulf of Cadiz slope current. J. Geophys. Res. 114, C03011 https://doi.org/10.1029/2008JC004771.

Peliz, A., Teles-Machado, A., Marchesiello, P., Dubert, J., Lafuente, J.G., 2009b. Filament generation off the Strait of Gibraltar in response to Gap winds. Dyn. Atmos. Ocean. 46, 36–45. https://doi.org/10.1016/j.dynatmoce.2008.08.002.

Pickett, M.H., 2003. Ekman transport and pumping in the California Current based on the U.S. Navy's high-resolution atmospheric model (COAMPS). J. Geophys. Res. 108, 3327. https://doi.org/10.1029/2003JC001902.

Relvas, P., Barton, E.D., 2005. A separated jet and coastal counterflow during upwelling relaxation off Cape São Vicente (Iberian Peninsula). Cont. Shelf Res. 25, 29–49. https://doi.org/10.1016/j.csr.2004.09.006.

Relvas, P., Barton, E.D., 2002. Mesoscale patterns in the Cape São Vicente (Iberian Peninsula) upwelling region. J. Geophys. Res. 107, 3164. https://doi.org/10.1029/2000JC000456.

Ribas-Ribas, M., Gómez-Parra, A., Forja, J.M., 2011. Air–sea CO2 fluxes in the north-eastern shelf of the Gulf of Cádiz (southwest Iberian Peninsula). Mar. Chem. 123, 56–66. https://doi.org/10.1016/j.marchem.2010.09.005.

Ruiz, J., Navarro, G., 2006. Upwelling spots and vertical velocities in the Gulf of Cádiz: an approach for their diagnose by combining temperature and ocean colour remote sensing. Deep. Res. Part II Top. Stud. Oceanogr. 53, 1282–1293. https://doi.org/10.1016/j.dsr2.2006.04.006.

Sánchez-Leal, R.F., Bellanco, M.J., Naranjo, C., García-Lafuente, J., González-Pola, C., 2020. On the seasonality of waters below the seasonal thermocline in the Gulf of Cádiz. Cont. Shelf Res. 204 https://doi.org/10.1016/j.csr.2020.104190.

Sánchez, R.F., Mason, E., Relvas, P., da Silva, A.J., Peliz, Á., 2006. On the inner-shelf circulation in the northern Gulf of Cádiz, southern Portuguese shelf. Deep Sea Res. Part II Top. Stud. Oceanogr. 53, 1198–1218. https://doi.org/10.1016/j.dsr2.2006.04.002.

Sánchez, R.F., Relvas, P., 2003. Spring–summer climatological circulation in the upper layer in the region of Cape St. Vincent, Southwest Portugal. ICES J. Mar. Sci. 60, 1232–1250. https://doi.org/10.1016/S1054-3139(03)00137-1.

Sánchez, R.F., Relvas, P., Delgado, M., 2007. Coupled ocean wind and sea surface temperature patterns off the western Iberian Peninsula. J. Mar. Syst. 68, 103–127. https://doi.org/10.1016/j.jmarsys.2006.11.003.

Santos, A.I.P. de O. da S., 2005. Caracterização Hidro-Sedimentológica Do Estuário Do Guadiana. M. S. Thesis. Universidade Técnica de Lisboa.

Silva, A.J. da, Santos, A.I., Garcia, A.C., González, R., 2008. Análise dos resultados referentes à segunda fase de execusção do projecto SIRIA: Dezembro 2000 - Dezembro 2001 e relatório final do projecto. Instituto Hidrográfico.

Simpson, J.H., Sharples, J., 2012. Introduction to the physical and Biological Oceanography of shelf seas. In: Introduction to the Physical and Biological Oceanography of Shelf Seas. Cambridge University Press, Cambridge, pp. 68–69. https://doi.org/10.1017/CBO9781139034098.

Teles-Machado, A., Peliz, Á., Dubert, J., Sánchez, R.F., 2007. On the onset of the gulf of Cadiz coastal Countercurrent. Geophys. Res. Lett. 34, L12601 https://doi.org/10.1029/2007GL030091.

Trenberth, K.E., Large, W.G., Olson, J.G., 1990. The mean annual Cycle in Global ocean wind stress. J. Phys. Oceanogr. 20, 1742–1760. https://doi.org/10.1175/1520-0485(1990)020<1742:TMACIG>2.0.CO;2.

Trigo, R.M., DaCamara, C.C., 2000. Circulation weather types and their influence on the precipitation regime in Portugal. Int. J. Climatol. 20, 1559–1581. https://doi.org/10.1002/1097-0088(20001115)20:13<1559::AID-JOC555>3.0.CO;2-5.

Vargas, J.M., García-Lafuente, J., Delgado, J., Criado, F., 2003. Seasonal and wind-induced variability of sea surface temperature patterns in the gulf of Cádiz. J. Mar. Syst. 38, 205–219. https://doi.org/10.1016/S0924-7963(02)00240-3.

Wang, D., 1997. Effects of small-scale wind on coastal upwelling with application to Point Conception. J. Geophys. Res. 102, 15555–15566. https://doi.org/10.1029/97JC00635.